SOLAR CELLS

Inactive $(PbI_2)_2RbCl$ stabilizes perovskite films for efficient solar cells

Yang Zhao[1,2], Fei Ma[1,2], Zihan Qu[1,2], Shiqi Yu[1,2], Tao Shen[2,3], Hui-Xiong Deng[2,3], Xinbo Chu[1,2], Xinxin Peng[4], Yongbo Yuan[4,5], Xingwang Zhang[1,2], Jingbi You[1,2]*

In halide perovskite solar cells the formation of secondary-phase excess lead iodide (PbI_2) has some positive effects on power conversion efficiency (PCE) but can be detrimental to device stability and lead to large hysteresis effects in voltage sweeps. We converted PbI_2 into an inactive $(PbI_2)_2RbCl$ compound by RbCl doping, which effectively stabilizes the perovskite phase. We obtained a certified PCE of 25.6% for $FAPbI_3$ (FA, formamidinium) perovskite solar cells on the basis of this strategy. Devices retained 96% of their original PCE values after 1000 hours of shelf storage and 80% after 500 hours of thermal stability testing at 85°C.

Several strategies can enhance the power conversion efficiency (PCE) of perovskite solar cells (PSCs), such as growing films with high crystallinity (*1*, *2*), doping with anions, cations, or both (*3*–*5*), engineering the charge transport layer (*6*–*12*), and use of a universal passivation layer (*13*–*16*). Several groups have reported certified PCEs >25% by modulating the SnO_2 electron transport layer (*10*–*12*).

Previous reports have shown that the secondary phase of PbI_2 is critical for attaining high performance levels (*7*, *12*, *17*–*24*). The benefits of excess PbI_2—either in the bulk or at the grain boundary of perovskite films—have mainly been attributed to its passivation effect resulting from the formation of a type-I band alignment (*24*). However, excess PbI_2 is too active and leads to instability of the device and large hysteresis in current density voltage (*J-V*) characteristics (*18*, *23*, *25*, *26*). Both factors can be ascribed to the photodecomposition of PbI_2 and the enhanced ionic migration.

It is crucial to manage excess unstable PbI_2 in perovskite films to achieve high efficiency. Recently, Luo *et al.* developed a ligand-modulation approach to manage the excess PbI_2 and successfully improved both PCE (up to 22%) and stability (*23*).

We propose stabilization of the perovskite by converting excess PbI_2 into an inactive, new, secondary-phase $(PbI_2)_2RbCl$ that can improve the stability of the perovskite $FAPbI_3$ layer (for simplicity, the perovskite film with $(PbI_2)_2RbCl$ is henceforth referred to as PIRC), in addition to improving its optoelectronic properties, the reduction of PbI_2 decreased the bandgap of the perovskite layer. As a result, a 26.1% efficiency (certification efficiency: 25.6%) of perovskite solar cells with >1000 hours of shelf stability and 500 hours of thermal stability at 85°C have been developed.

We deposited nearly pure $FAPbI_3$ by a modified two step method used in our previous reports (*7*, *15*, *18*). For deposition of $FAPbI_3$, the PbI_2 seed layer was first grown on the substrate while the organic salt formamidinium iodide (FAI) solution was deposited on PbI_2 for diffusion and formation of perovskite by annealing. Further, to improve the perovskite crystallization, methylammonium chloride (MACl) was added to the FAI solution (*7*, *27*). In contrast to our previous reports, to enhance the thermal stability and decrease the bandgap of perovskite as much as possible, traditional organic salt methylammonium iodide (MAI) or methylammonium bromide was not used in this study. We confirmed that a 5% molar ratio of RbCl doping is the best condition for device performance, as discussed below.

We performed scanning electron microscopy (SEM) (Fig. 1, A and B) measurements to determine the perovskite film crystallinity. For the control film, the perovskite crystal grain size was ~1 μm and the grains were surrounded by PbI_2 grains (white needle shapes, Fig. 1A), which formed as decomposition products on the perovskite surface after heating at elevated temperatures. For the PIRC films, the perovskite crystal size was increased to ~2 μm. Instead of a large fraction of evenly distributed white needle-shaped grains, sporadically distributed white irregular flakes were observed (Fig. 1B). Energy dispersive spectroscopy mapping of the PIRC film (fig. S1) revealed that the white region contained Pb, I, Rb, and Cl, but no N. This result indicated that there was

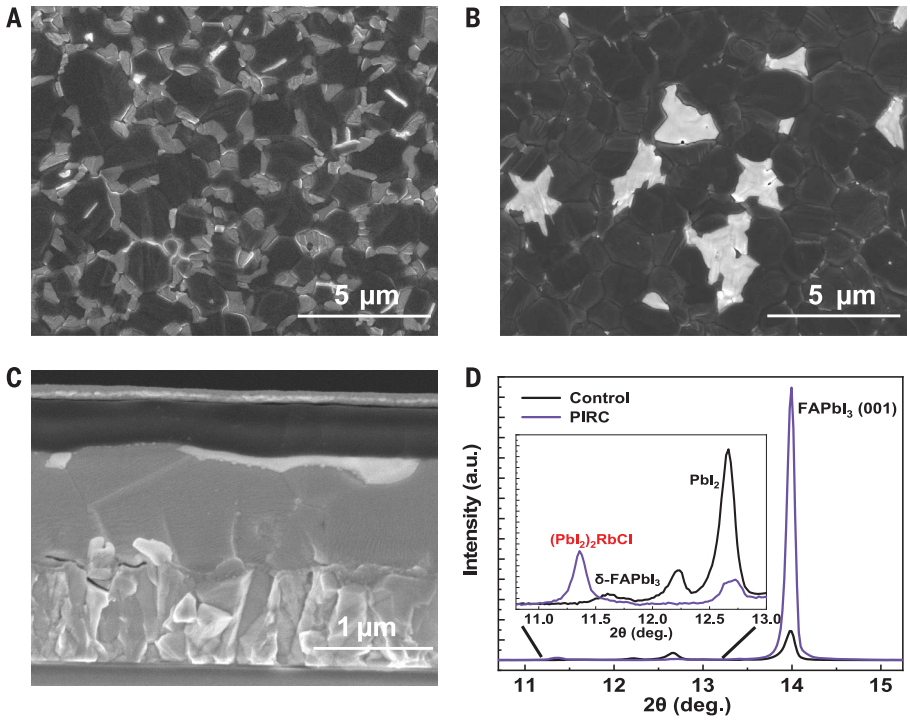

Fig. 1. Microstructures and morphology of secondary-phase $(PbI_2)_2RbCl$ on perovskite. (**A** and **B**) SEM of perovskite films without RbCl and with 5% RbCl, respectively. Scale bars, 5 μm. (**C**) Cross-section SEM image of a completed device using RbCl doped perovskite. Scale bar, 1 μm. (**D**) XRD of perovskite without RbCl and with 5% RbCl.

[1]Key Laboratory of Semiconductor Materials Science, Institute of Semiconductors, Chinese Academy of Sciences, Beijing, P.R. China, 100083. [2]Center of Materials Science and Optoelectronics Engineering, University of Chinese Academy of Sciences, Beijing, P.R. China, 100049. [3]State Key Laboratory of Superlattices and Microstructures, Institute of Semiconductors, Chinese Academy of Sciences, Beijing, P.R. China, 100083. [4]Hunan Key Laboratory of Super Microstructure and Ultrafast Process, School of Physics and Electronics, Central South University, Changsha, Hunan, P.R. China, 410083. [5]Hunan Key Laboratory of Nanophotonics and Devices, School of Physics and Electronics, Central South University, Changsha, Hunan, P.R. China, 410083.
*Corresponding author. Email: jyou@semi.ac.cn

no organic-inorganic hybrid $FAPbI_3$ perovskite phase in this region whereas a PbI_2/RbCl mixed phase was possible (fig. S1 and tables S1 and S2). The cross-section SEM images showed that the new secondary phases only formed on top of the perovskite films (Fig. 1C).

Conventional x-ray diffraction (XRD) for the perovskite films (Fig. 1D) showed that the main diffraction peak of the control film could be assigned from the black phase of $FAPbI_3$ located at 14°. The yellow phase of $FAPbI_3$ (11.7°) was also observed in addition to the PbI_2 diffraction peak (12.6°) (the inset of Fig. 1D shows the enlarged figure). The PbI_2 diffraction peak in the PIRC film was largely suppressed and a diffraction peak (11.3°) emerged (Fig. 1D, inset). Grazing-incidence wide-angle x-ray scattering (GIWAXS) of the PIRC films were also consistent with conventional XRD results (fig. S2). We directly compared the XRD pattern of the annealed PbI_2/RbCl precursor films with different ratios (fig. S3), and we found that the diffraction of PbI_2 almost disappeared whereas the diffraction intensity at 11.3° was greatly enhanced when the ratio of PbI_2/RbCl is 2. Thus, we could attribute the 11.3° peak to crystalline $(PbI_2)_2RbCl$. Density function theory calculations and powder diffraction results also confirmed this assignment (fig. S4).

To study the phase stability of the perovskite materials obtained we aged the perovskite films at 85°C for 48 hours. The XRD and SEM results showed that more PbI_2 was formed after heating of the control perovskite film (figs. S5 and S6). We found that integration of the XRD intensity ratio of PbI_2/perovskite in the control film increased from 0.42 to 0.98 after aging whereas the PIRC film remained at ~0.10. These results indicate that excess PbI_2 can

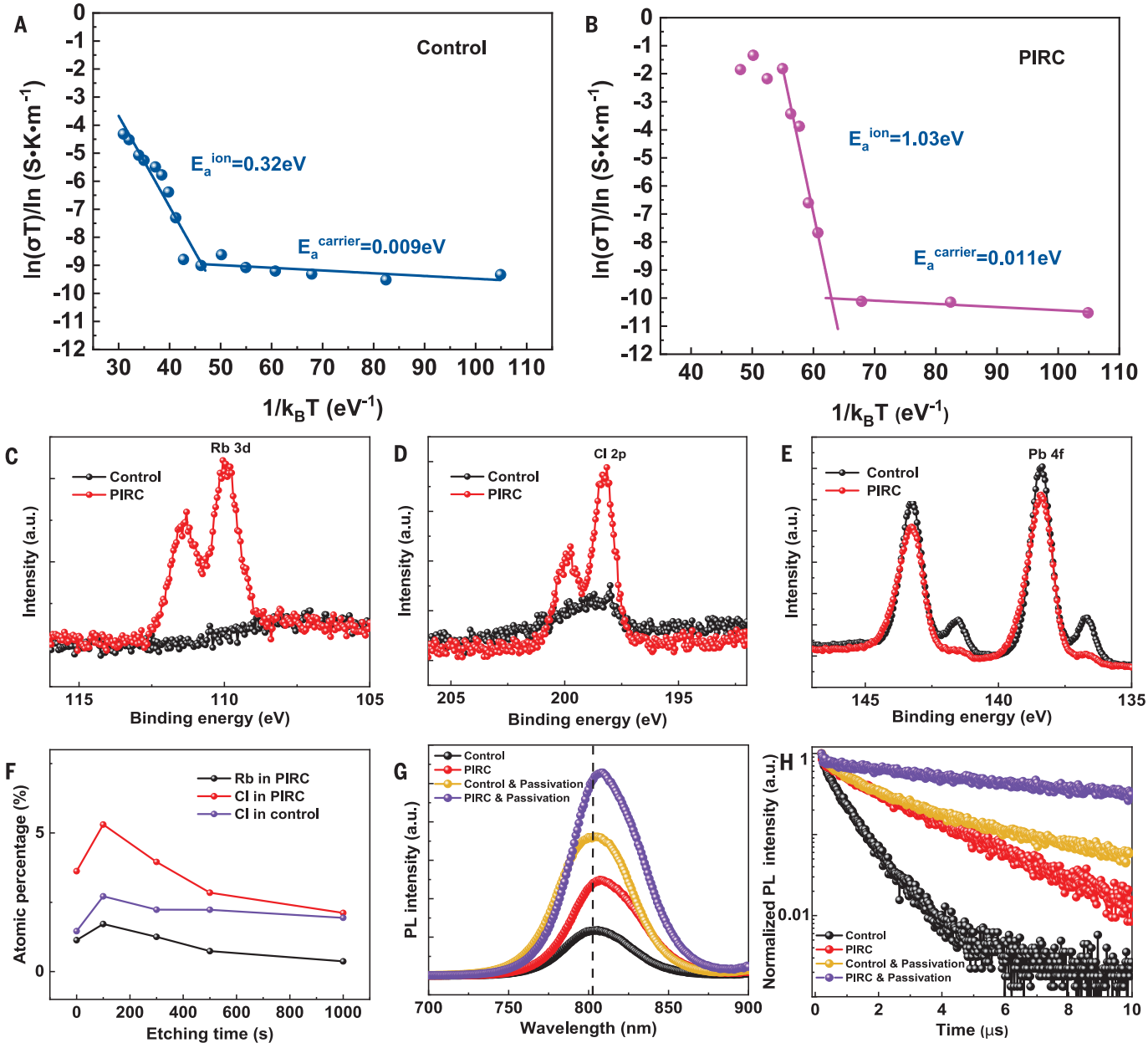

Fig. 2. Properties of control and PIRC perovskite films including ion transport, composition, and photoluminescence. (**A** and **B**) Temperature-dependent conductivity measurements of control and PIRC perovskite films, respectively. (**C** to **E**) XPS spectra of Rb 3d, Cl 2p, and Pb 4f core energy levels in control and PIRC films, respectively. (**F**) XPS depth profile of Cl in the control and PIRC samples; the Rb depth in the PIRC sample is also included. (**G** and **H**) Steady PL and TRPL of control perovskite film, PIRC film, and their surface passivation films.

trigger decomposition of the perovskite layer (*18*, *25*, *26*, *28*, *29*) whereas the perovskite becomes much more stable after conversion of PbI_2 into the $(PbI_2)_2RbCl$ phase.

The presence of PbI_2 in the perovskite layer could lead to ion migration as a result of the formation of Schottky defects such as FA and I vacancies (*30*). We measured the temperature-dependent conductivity with a previously reported procedure (*31*) to confirm that ion migration is suppressed in the PIRC films through reduction of PbI_2 (Fig. 2, A and B). We can estimate the ion migration active energy based on the Nernst-Einstein relation:

$$\sigma T = \sigma_0 \exp(-E_a/k_B T)$$

where σ_0 is a constant, k_B is Boltzmann's constant, σ is ionic conductivity, T is temperature, and E_a is the ion-migration activation energy. We derived E_a values from the slope of the ln (σT) versus $1/T$ of ~0.32 eV for the control films and ~1.03 eV for the PIRC films. Given the E_a, we can estimate that the ion migration rates (k) at the operating temperature (50°C) are 4.2×10^8 s^{-1} and 3.3×10^{-3} s^{-1}, respectively, based on the Arrhenius equation:

$$k = (k_B T)/h \exp(-E_a/RT)$$

where k_B stands for the Boltzmann constant, T is temperature, h is the reduced Planck constant, and R is the ideal gas constant (*32*). We found that $(PbI_2)_2RbCl$ could not easily react with FA cations or I ions compared with those of PbI_2 (fig. S7), inferring that $(PbI_2)_2RbCl$ lacks similarity to PbI_2 in regards to acting as a sink for absorbing adjacent FA and I during heating, photo soaking, or voltage application. This will suppress FA and I vacancy formation, as well as ion migration. Another possible reason for suppression of ion migration as a result of $(PbI_2)_2RbCl$ is that as the derivative of PbI_2, the $(PbI_2)_2RbCl$ is a fully intercalated compound (fig. S4) with narrow ion migration pathways whereas PbI_2 is a layer structure crystal with enough interlamellar space for ion migration.

X-ray photoelectron spectroscopy (XPS) characterization of the PIRC film showed the expected Rb 3d core level peak (Fig. 2C). For Cl, a substantial difference was found between the control and PIRC films. We estimated ~2.7% Cl in the control film (Fig. 2D), resulting from the addition of residual MACl during perovskite film growth, although most MACl would have evaporated during annealing. In these perovskite films, the radius of Cl was too small to incorporate into the lattice. We estimated that ~5.3% Cl was left in the PIRC film that was bonded with Pb or Rb ions and could not be easily evaporated (Fig. 2D). This excess Cl could stabilize the perovskite phase through strong Pb-Cl bonding (*8*–*10*). The presence of RbCl also enhanced the formation of the black

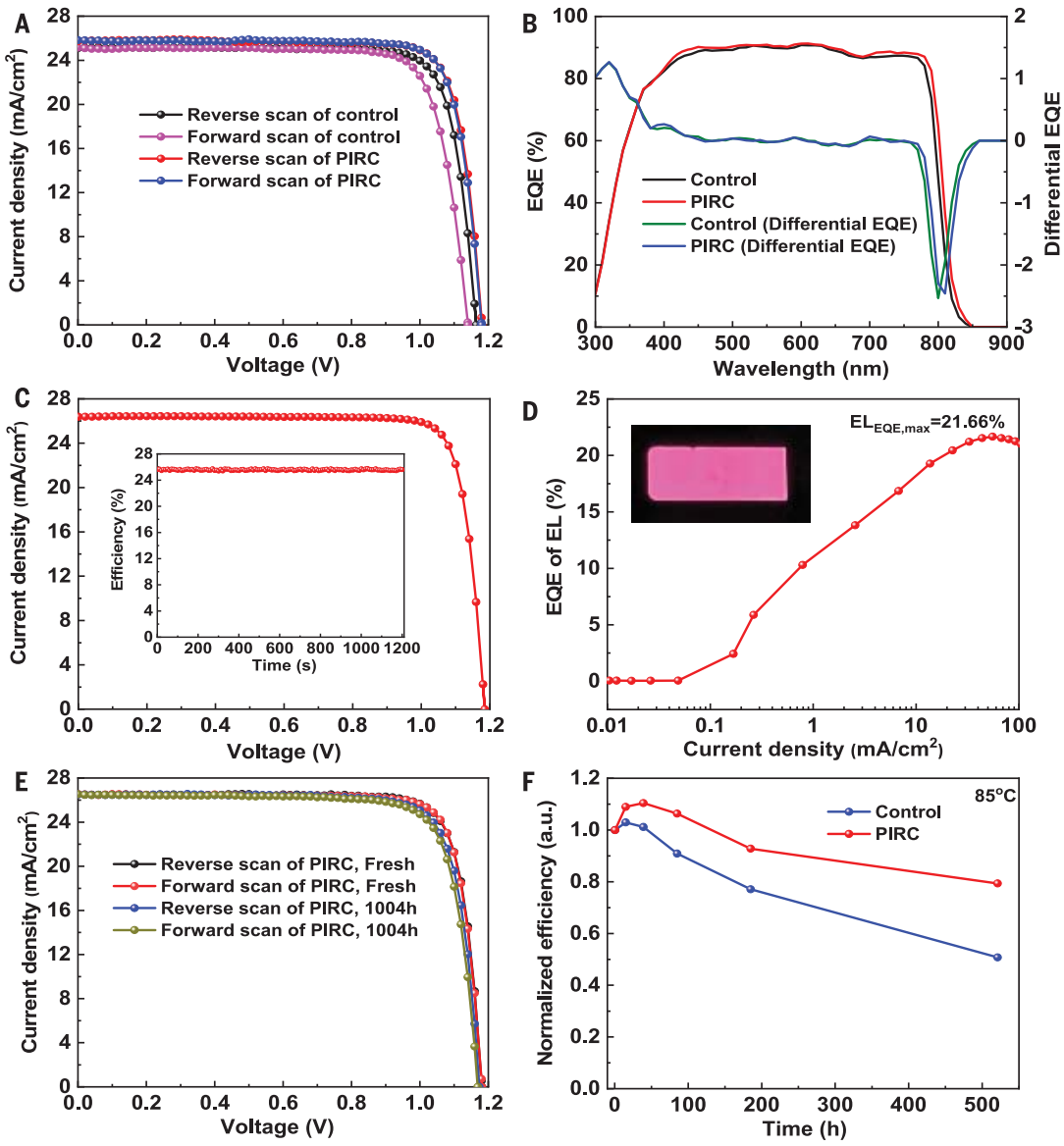

Fig. 3. Device characteristics and accelerated stability tests. (**A**) The typical *J-V* curves of the control and PIRC-based devices under one-sun (100 mW/cm^2) conditions. Both the reverse and forward scans are included. (**B**) EQE of devices for control and PIRC-based devices. (**C**) Best device performance based on PIRC films. (Inset) MPP of the device. (**D**) EQE of electroluminescence of the PIRC-based devices while operating as light-emitting diodes. (Inset) EL image of the device. (**E**) *J-V* curves of the PIRC-based device before and after aging in a nitrogen environment for 1004 hours. (**F**) Thermal stability (85°C) of the control and PIRC-based devices.

perovskite phase (Fig. 1D). Previous studies showed that the metallic Pb formed from PbI_2 under high-energy illumination drives loss of I_2 (*28*, *29*). We found that the metallic state of Pb was suppressed after introducing PIRC (Fig. 2E), which could be due to much better photo stability of PIRC compared with PbI_2 (fig. S8).

Depth profile XPS for the PIRC films revealed that the top surface was Rb- and Cl-rich (Fig. 2F and fig. S9), which could be a result of the secondary phase having a different solubility in the precursor solvent. Time-of-flight second ion mass spectroscopy (ToF-SIMS) of the control and target perovskite films (fig. S10) also confirmed that Rb and Cl that convert PbI_2 into $(PbI_2)_2RbCl$ were mainly distributed on top of the perovskite. The Cl ratio on the bottom of the perovskite is about 1% higher than that in the bulk estimated from ToF-SIMS (fig. S10) and XPS results (Fig. 2F).

Excess PbI_2 can increase the perovskite bandgap (*7*, *12*, *17*), which could be attributed to the strong quantum confinement in perovskite/PbI_2. The photoluminescence (PL) emission of the control film peak at 805 nm red shifted to 810 nm in the PIRC film (Fig. 2G). The PIRC perovskite film showed enhanced PL intensity indicative of suppression of nonradiative recombination. Time-resolved photoluminescence (TRPL) showed that the lifetime of the perovskite increased from 0.98 μs to 2.3 μs for the PIRC films and that this lifetime can be extended to ~6 μs with the addition of a passivation layer on the perovskite surface (Fig. 2H).

We fabricated the solar cell devices in an n-i-p configuration of FTO/SnO_2/perovskite/passivation layer/Spiro-OMeTAD/Au [FTO, fluorine-doped tin oxide; spiro-OMeTAD, 2,2′,7,7′-tetrakis(N,N-dipmethoxyphenylamine)-9,9′-spirobifluorene; Fig. 1C]. After testing the device performance using perovskite films with 1 to 10% RbCl doping we found that the 5% RbCl device had the best performance (fig. S11 and table S3); additionally, improved performance was observed when Cl was used as the halide (fig. S12 and table S4). A representative *J-V* curve for the control and 5% RbCl-doped device showed that each of the photovoltaic parameters increased (Fig. 3A). The typical short circuit current density (J_{SC}) increased from 25.1 to 25.8 mA/cm^2, which could be attributed mainly to the lower bandgap (Fig. 2G) as well as the external quantum efficiency (EQE) (Fig. 3B). The open circuit voltage V_{OC} increase from 1.17 to 1.19 eV despite the bandgap decrease was due to the suppression of recombination. The fill factor (FF) was almost the same or slightly improved compared with the control device.

Overall, the PCE increased from 24.6 to 25.6%. In addition, the PIRC-based device was almost hysteresis-free whereas the control device showed obvious hysteresis. The highest PCE for an optimized device tested in our laboratory was 26.1% (Fig. 3C); said device also showed 25.7% efficiency and steady output for 1200 s (device area: 0.108 cm^2; measurement mask size: 0.0741 cm^2). The statistics of the PCE distribution confirm the reproducibility of our results (fig. S13). These devices, which showed 25.6% certificated efficiency with a V_{OC} of 1.182 V, a J_{SC} of 26.3 mA/cm^2, and a *FF* of 82.7% (figs. S14 and S15), were sent to the accredited laboratory in Newport, USA, for certification.

The V_{OC} reflects the recombination rate of a given device and can be measured through the EQE at short circuit current conditions when the device is tested as a light-emitting diode. These devices had electroluminescence (EL) efficiencies as high as 21.6% under the injection current of 26 mA/cm^2 (equal to short circuit current J_{ph}) (Fig. 3D). High quantum efficiency can only be observed through charge confinement in light-emitting diodes, so the high-EL efficiency indicates that the defect-related nonradiative recombination was largely suppressed in the tested device. Light intensity–dependent results (fig. S16) also confirm this conclusion (*33*) and are consistent with our device simultaneously delivering high J_{sc} and V_{oc}.

We tracked device shelf stability and hysteresis in a nitrogen environment while using the Spiro-OMeTAD as the hole transport layer. After 1004 hours of aging, a slight drop in the FF from 82.6 to 80.6% was observed for the RPIC strategy–based device, which could be attributed to the reduction of Spiro-OMeTAD in an oxygen-free environment (*34*, *35*); further, it had 96% of its original PCE. The device maintained almost the same PCE in both reverse and forward scans (Fig. 3E). However, the control device could only maintain its reverse scan PCE of 24.1% whereas the forward efficiency was reduced to 22.9%. We attributed this enhanced hysteresis (fig. S17 and table S5) to the spontaneous formation of PbI_2 as a result of aging and enhanced ion migration.

We also tested accelerated aging stability while heating the devices at 85°C in a nitrogen environment. We removed other possible sources of instability such as the organic passivation layer and replaced Spiro-OMeTAD with Poly[bis(4-phenyl)(2,4,6-trimethylphenyl)amine]. We found that the PIRC-targeted devices primarily showed improved stability. Under 500 hours of continuous heating, the device maintained 80% initial performance (Fig. 3F and table S6) whereas the control device only retained 50% of its initial PCE. The PIRC method proposed in this study could enhance both stability and device efficiency which will provide a new direction and push the development of perovskite solar cells; there is also potential for use in other optoelectronic devices such as light-emitting diodes and photodetectors.

REFERENCES AND NOTES

1. N. J. Jeon *et al*., *Nat. Mater.* **13**, 897–903 (2014).
2. D. Bi *et al*., *Nat. Energy* **1**, 16142 (2016).
3. N. J. Jeon *et al*., *Nature* **517**, 476–480 (2015).
4. Y. H. Lin *et al*., *Science* **369**, 96–102 (2020).
5. M. Saliba *et al*., *Science* **354**, 206–209 (2016).
6. H. Zhou *et al*., *Science* **345**, 542–546 (2014).
7. Q. Jiang *et al*., *Nat. Energy* **2**, 16177 (2016).
8. H. Tan *et al*., *Science* **355**, 722–726 (2017).
9. Y. Wang *et al*., *Science* **365**, 687–691 (2019).
10. H. Min *et al*., *Nature* **598**, 444–450 (2021).
11. M. Kim *et al*., *Science* **375**, 302–306 (2022).
12. J. J. Yoo *et al*., *Nature* **590**, 587–593 (2021).
13. X. Zheng *et al*., *Nat. Energy* **2**, 17102 (2017).
14. D. Luo *et al*., *Science* **360**, 1442–1446 (2018).
15. Q. Jiang *et al*., *Nat. Photonics* **13**, 460–466 (2019).
16. R. Wang *et al*., *Science* **366**, 1509–1513 (2019).
17. D. Bi *et al*., *Sci. Adv.* **2**, e1501170 (2016).
18. Q. Jiang *et al*., *Adv. Mater.* **29**, 1703852 (2017).
19. L. Wang, C. McCleese, A. Kovalsky, Y. Zhao, C. Burda, *J. Am. Chem. Soc.* **136**, 12205–12208 (2014).
20. B. W. Park *et al*., *Nat. Commun.* **9**, 3301 (2018).
21. T. J. Jacobsson *et al*., *J. Am. Chem. Soc.* **138**, 10331–10343 (2016).
22. C. J. Tong, L. Li, L. Liu, O. V. Prezhdo, *ACS Energy Lett.* **3**, 1868–1874 (2018).
23. H. Wang *et al*., *Adv. Mater.* **32**, 2000865 (2020).
24. Q. Chen *et al*., *Nano Lett.* **14**, 4158–4163 (2014).
25. F. Liu *et al*., *Adv. Energy Mater.* **6**, 1502206 (2016).
26. J. Holovsky *et al*., *ACS Energy Lett.* **4**, 3011–3017 (2019).
27. M. Kim *et al*., *Joule* **3**, 2179–2192 (2019).
28. R. K. Gunasekaran *et al*., *ChemPhysChem* **19**, 1507–1513 (2018).
29. J. Schoonman, *Chem. Phys. Lett.* **619**, 193–195 (2015).
30. H. Yu, H. Lu, F. Xie, S. Zhou, N. Zhao, *Adv. Funct. Mater.* **26**, 1411–1419 (2016).
31. J. Zhao *et al*., *Sci. Adv.* **3**, eaao5616 (2017).
32. J. M. Azpiroz, E. Mosconi, J. Bisquert, F. D. Angelis, *Energy Environ. Sci.* **8**, 2118–2127 (2015).
33. G. J. Wetzelaer *et al*., *Adv. Mater.* **27**, 1837–1841 (2015).
34. W. H. Nguyen, C. D. Bailie, E. L. Unger, M. D. McGehee, *J. Am. Chem. Soc.* **136**, 10996–11001 (2014).
35. B. Tan *et al*., *Adv. Energy Mater.* **9**, 1901519 (2019).

ACKNOWLEDGMENTS

We thank Y. Yang from the Shanghai Synchrotron Radiation Facility (SSRF), the Shanghai Institute of Applied Physics, Chinese Academy of Sciences for GIWAXIS measurements; we also thank W. Ke from Wuhan University for discussions regarding the PbI_2 complex, and Z. Chu from the Institute of Semiconductors, Chinese Academy of Sciences, for helping with the electroluminescence measurements. **Funding:** J.Y. was supported by National Key Research and Development Program of China (2020YFB1506400) and National Natural Science Foundation of China (61925405, 61634001). H.D. was supported by National Natural Science Foundation of China (61922077) and Y.Y. was supported by Innovation-Driven Project of Central South University (2020CX006). **Author contributions:** J.Y. and Y.Z. conceived the idea; Y.Z. fabricated and characterized the devices; F.M. and Z.Q. participated in device fabrication and preparation for certification; T.S. and H.D. conducted the crystal structure simulation; X.P. and Y.Y. carried out the ion migration activation measurements; F.M., Z.Q., S.Y., X.C., and X.Z. were involved in the data analysis. J.Y. directed and supervised the project, X.Z. cosupervised the project, and J.Y. and Y.Z. cowrote the manuscript. All authors contributed to discussions and finalizing the manuscript. **Competing interests:** A Chinese patent application (CN 202210471109.8) was submitted by the Institute of Semiconductors, Chinese Academy of Sciences, that covers the $(PbI_2)_2RbCl$ used in stabilizing the perovskite. **Data and materials availability:** All data needed to evaluate the conclusions in the paper are present in the paper or the supplementary materials.

SUPPLEMENTARY MATERIALS

science.org/doi/10.1126/science.abp8873
Materials and Methods
Supplementary Text
Figs. S1 to S17
Tables S1 to S6
References (*36*–*45*)
Movie S1

Submitted 4 March 2022; accepted 27 June 2022
10.1126/science.abp8873

Inactive (PbI2)2RbCl stabilizes perovskite films for efficient solar cells

Yang ZhaoFei MaZihan QuShiqi YuTao ShenHui-Xiong DengXinbo ChuXinxin PengYongbo YuanXingwang ZhangJingbi You

Science, 377 (6605), • DOI: 10.1126/science.abp8873

Managing excess lead iodide

In hybrid perovskite solar cells, the formation of lead iodide (PbI2) can provide some passivation effects but can lead to device instability and hysteresis in current–density changes with voltage. Zhao *et al*. show that doping with rubidium chloride (RbCl) can create a passive inactive (PbI)RbCl phase that stabilizes the perovskite phase and lowers its bandgap. Devices exhibited 25.6% certified power efficiency and maintained 80% of that efficiency after 500 hours of operation at 85°C. —PDS